

Acoustic Fault Detection Technique for High-Power Insulators

Kyu-Chil Park, Yuichi Motai, *Senior Member, IEEE*, and Jong Rak Yoon

Abstract—Insulators are important equipment used to electrically isolate and mechanically hold wires in high-voltage power transmission systems. Faults caused by the deterioration of the insulators induce very serious problems to the power transmission line. Techniques were introduced for the acoustic detection of insulator faults by acoustic radiation noises. Radiation noises were measured from normal state insulators and fault state insulators in an anechoic chamber. The insulators used were two porcelain insulators, a cut-out switch, two line posters, and a lightning arrester. A new acoustic technique determines the direction of the insulator faults using source localization with three-dimensional microphone arrays. The advantage is to classify the fault state insulators without human inspection by considering the amount of total noises and 120-Hz harmonic components. The fault detection was determined by neural network to diagnose the state automatically. The proposed technique was evaluated by distinct, real datasets and the efficacy was validated. The noise source was detected with 100.0% accuracy and the classification ratio achieved 96.7% for three typical conditions.

Index Terms—Insulator, neural network (NN), peak detection, radiation noise, source localization.

I. INTRODUCTION

INSULATORS are used for the mechanical holding of the wires and the electrical insulating in the transmission line system. Since the failure of such insulators causes a large barrier to having a high-quality power supply, the detection of insulator faults is necessary for improving the stability and reliability of the power system for replacement or diagnosis [1]–[5]. The insulator failures are mainly classified problems caused by microscopic defects or cracks in the manufacturing process or by deterioration due to lightning, cold, or salinity after installation on power plants. The problem of the manufacturing process is detected upon sufficient inspection before the installation, but

the problem of the deterioration after the installation requires periodic diagnosis.

Looking at the breakdown process simply, it is known that the insulator is aging, or damaged so that feeble discharge occurs, then electrical destruction of the oxide ensues, and finally the isolation of insulators is destroyed. As the thickness of the insulator's oxide film is between 0.001 and 0.01 in, a breakdown process is defined as a microspark, not arc or spark. It is known that the breakdown occurs when the voltage is larger than the threshold voltage of the oxide film's breakdown voltage [1]–[3]. The methods for detecting a faulty isolation insulator with deterioration use voltage division and the insulation resistance, the electric field, ultrasonic waves, an infrared/ultraviolet sensor camera, and so on [2], [3]. Each method has advantages and disadvantages in the reliability of the detection results, detecting times, price, or stability. Since an insulator suffers from various issues, it is difficult to determine the best measurement method to cover the varieties of all the faults. The advantage is to classify the fault state insulators without human inspection.

There is a noise source detection system using a microphone array in [2]. As it has three microphones to estimate the three-dimensional (3-D) position of the fault insulator, it measures the noises twice at two different measurement positions, and reconstructs six microphones' data processing to represent the noise source position. Since our system has four microphone array in 3-D structure, it is possible to estimate the noise position with just one time measurement.

This paper demonstrates the effective capability of the combination of acoustic source detection and fault detection. The demanding problem of how to automatically determine the status of a power insulator is solved by developing an acoustic sensor system. A sound detection system mounted to a robot operating on the top of the pole wires, using measurement and analysis of the radiated noise from the insulator, was developed. Six insulators were measured and analyzed—two porcelain insulators (PIs), a cut-out switch (COS), two line posters (LPs), and a lightning arrester. For comparison, the radiated noise was measured from a normal state insulator and a fault state insulator, then the frequency spectrum characteristics were analyzed so that it could be determined whether the insulator faulted.

This paper is organized as follows. In Section II, the relevant studies are listed. In Section III, the proposed insulator noise detection techniques are presented in detail. Section IV presents and discusses experimental results of proposed methods. A summary of the performance of the proposed method is presented in Section V.

Manuscript received November 30, 2016; revised April 4, 2017, April 27, 2017, and May 8, 2017; accepted May 17, 2017. This work was supported in part by the Pukyong National University Research Abroad Fund in 2015 (C-D-2015-0514), and in part by the National Science Foundation under Grant 1054333. (Corresponding author: Yuichi Motai.)

K.-C. Park and J. R. Yoon are with the Department of Information and Communications Engineering, Pukyong National University, Busan 608-737, South Korea (e-mail: kcpark@pknu.ac.kr; jryoon@pknu.ac.kr).

Y. Motai is with the Electrical Engineering Department, Virginia Commonwealth University, Richmond, VA 23284 USA (e-mail: ymotai@vcu.edu).

Color versions of one or more of the figures in this paper are available online at <http://ieeexplore.ieee.org>.

Digital Object Identifier 10.1109/TIE.2017.2716862

TABLE I
REPRESENTATIVE STUDIES ON FAULT DIAGNOSIS SYSTEMS

Category	Representative studies and characteristics
Transient [6]	Optimize the transient response of proportional-resonant current controllers.
Imbalance [7]	Stationary-frame control for voltage unbalance compensation in an islanded microgrid.
Waveform Distortion [8]–[10]	Adaptive linear network for harmonic and interharmonic estimation.
Fault monitoring [11]–[13]	Reduce the tracking error and compensate harmonics of the inverter systems.
	Selective harmonic detection system.
	Adaptive multiscale noise for a health diagnosis under stochastic resonance conditions.
	Phase control scheme based on diagnosis of energy conversion system.
	Real-time algorithm to monitor electric motors.

II. RELEVANT STUDIES

The relevant studies are listed as fault diagnosis in Section II-A, noise source from the power line system in Section II-B, and array signal processing in Section II-C.

A. Fault Diagnosis

The monitoring of delivering electric power is affected by all equipment used for each specific domain. Fault diagnosis is evaluated by a set of electrical boundaries that allows a piece of equipment to function in its intended manner without significant loss of performance or life expectancy [4]. IEEE 1159 defines the power quality as the significant factor in [5].

Table I lists the representative studies on variations of power quality that may be used for fault diagnosis. To provide categories and typical characteristics of power system electromagnetic phenomena, power quality is affected by significant phenomena such as transients [6], imbalance [7], and waveform distortion [8]–[10]. The adaptive multiscale noise for a health diagnosis is developed [11], and real-time monitoring for electric motors can detect fault signatures effectively [12], [13].

B. Noise Source From the Power Line System

The noise source of the power line system is very diverse, but can be divided into main noise sources and minor noise sources [1], [2]. Table II shows the main noise sources. These radiated noises from the noise sources are generated by one independent noise source or in combination with other noise sources. The installation of the hardware components used for power companies is different, and the characteristics of the noise sources may vary from concrete/wood poles, and coated/noncoated wire ties. The noise sources of the power line system are complex, and consequently, they may be independent/dependent. Knowledge of the entire power line system is required to take appropriate measures in detecting them.

The bell insulator is one of the main targets of this study. Its average lifetime is 40 years. However, as it is a major source of noise, it becomes replaced by any other type of insulator. The

TABLE II
MAIN NOISE SOURCE OVER WIRE SYSTEM [1]

Rating	Source hardware
1	Bell insulator
2	Loose hardware
2	Lightning arrester
3	Insulated tie wires or bare tie wires on insulated conductors
3	Small discharges between inadequately spaced and unbonded metal components
3	Improperly assembled transitions between overhead conductors and underground lines

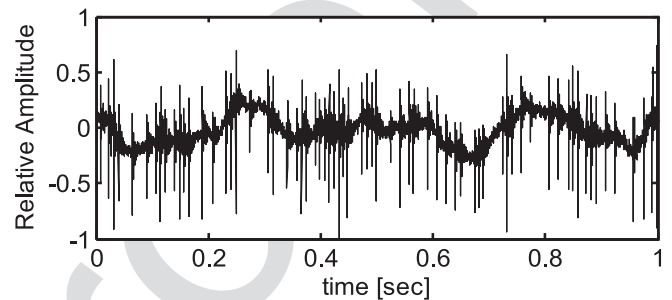


Fig. 1. Fault state insulator's time signal measured. It contains lots of spike signals. The period of the impulse groups is 8.3 or 16.6 ms according to the frequency of the electric voltage.

noise of the bell insulator is related to the electrical breakdown of the oxide film on the surface of the insulator. The complicated fracture process is well identified on the basis of the circuit.

The thickness of the oxide film of the insulator is from 0.001 to 0.01 in, so the destructive process is not considered to be an arc or spark. It is defined as microsparks when the threshold voltage is larger than the breakdown voltage of the oxide film. It may be intensified by the addition of radio signals, lightning, and other transient voltage switching on the normal transmission voltage. Fig. 1 shows a time signal in a fault state of an insulator. If it takes place on the maximum or minimum value of the transmission voltage, impulse groups may be generated at a period of 16.6 ms.

It can be concluded that noise due to the noise source of the power line system represents a form of impulse like the microspark. Also, the period of the impulse groups is 8.3 or 16.6 ms according to the frequency of the electric voltage.

C. Array Signal Processing

The array signal processing techniques are used to identify the acoustic characterization or estimate the position of the noise source by the receiving signals with sensor arrays in space [14]. It has been widely adopted on military sonar, medical ultrasound diagnostic equipment, and vehicle noise detection equipment. The array processing techniques [15] on these devices are adopted from the beamforming method [16], MUSIC method [17], correlation function method [18], bispectrum method [19], sound intensity method [20], acoustic holography method [21], and so on. They are each determined if the

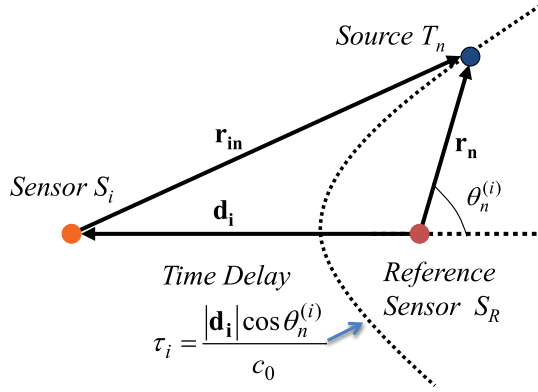


Fig. 2. Pair of sensors, sound source, and path length difference. The relative time delay can be estimated in a 2-D sensor system. The dots show the same time delay between two sensors.

149 application is in accordance with sound environment and pur-
 150 pose. The beamforming method and MUSIC method cannot
 151 be adopted because of the long distance detection on the tar-
 152 get with narrow-band signal. The spatial measuring range of
 153 the sound intensity method and acoustic holography method is
 154 wide so that the robot's geometric size becomes large. It cannot
 155 be attached to a robot, and required a long computation time in
 156 long-term measured data. In this study, a correlation function
 157 method employs a technique to estimate the position of the fault
 158 insulators.

159 III. INSULATOR NOISE DETECTION

160 The proposed insulator noise detection consists of the fol-
 161 lowing four modules. Cross-correlation function analysis of the
 162 array sensor received signal in Section III-A, noise source lo-
 163 cation estimation and arrangement in Section III-B, angular
 164 resolution and the grid size of the image plane in Section III-C,
 165 and the feature extraction techniques and neural network (NN)
 166 in Section III-D.

167 A. Cross-Correlation Function Analysis of the Array 168 Sensor Received Signal

169 Considering two receivers as shown in Fig. 2, they assumed
 170 abnormal noises from insulators as uncorrelated broadband
 171 noise sources. Assuming that the reference sensor is at the coor-
 172 dinate origin, each position and volume velocity are defined as
 173 r_n and $Q_n(t)$ ($n = 1, 2, \dots, N$), respectively. The measured
 174 sound pressures on the reference sensor and the arbitrary ith
 175 sensor is given by

$$176 \quad P_0(t) = \sum_{n=1}^N \frac{\rho Q_n \left(t - \frac{|\mathbf{r}_n|}{c_0} \right)}{4\pi |\mathbf{r}_n|}, \quad P_i(t) = \sum_{n=1}^N \frac{\rho Q_n \left(t - \frac{|\mathbf{r}_{in}|}{c_0} \right)}{4\pi |\mathbf{r}_{in}|} \quad (1)$$

176 where $\mathbf{r}_{in} = \mathbf{r}_n - \mathbf{d}_i$ and the bold lower case denotes the vec-
 177 tor. N , ρ , c_0 , and $|\bullet|$ are the number of the noise sources, the
 178 density of air, the sound speed on air, and the norm, respectively.

From (1), the cross-correlation function $R_i(\tau)$ is given by [19] 179

$$180 \quad R_i(\tau) = \int_{-\infty}^{\infty} P_0(t) P_i(t + \tau) dt$$

$$181 \quad = \int_{-\infty}^{\infty} \sum_{n=1}^N \sum_{m=1}^N \frac{\rho^2 Q_n \left(t - \frac{|\mathbf{r}_n|}{c_0} \right) Q_m \left(t - \frac{|\mathbf{r}_{im}|}{c_0} + \tau \right)}{16\pi^2 |\mathbf{r}_n| |\mathbf{r}_{im}|} dt \quad (2)$$

182 Defining $D_{nm}(\tau)$ for the cross-correlation function between
 183 the n th and m th noise source, we obtain

$$184 \quad D_{nm}(\tau) = \int_{-\infty}^{\infty} \rho^2 Q_n(t) Q_m(t + \tau) dt. \quad (3)$$

185 Since each source of noise is uncorrelated

$$186 \quad D_{nm}(\tau) = \begin{cases} D_n(\tau) \neq 0, & \text{if } n = m, \\ 0, & \text{if } n \neq m. \end{cases} \quad (4)$$

187 Equation (2) by (3) and (4) is converted into the following
 188 equation:

$$189 \quad R_i(\tau) = \sum_{n=1}^N \frac{D_n \left(\tau - \frac{|\mathbf{r}_{in}| - |\mathbf{r}_n|}{c_0} \right)}{16\pi^2 |\mathbf{r}_n| |\mathbf{r}_{in}|}$$

$$190 \quad = \sum_{n=1}^N A_n D_n \left(\tau - \frac{|\mathbf{d}_i| \cos \left(\theta_n^{(i)} \right)}{c_0} \right) \quad (5)$$

191 where $A_n = 1/(16\pi^2 |\mathbf{r}_n| |\mathbf{r}_{in}|)$. $\theta_n^{(i)}$ ($n = 1, 2, \dots, M$) is
 192 the angular position forming between a straight line on the re-
 193 ceivers and the n th noise source, as shown in Fig. 2. Therefore,
 194 the cross-correlation function of (5) will have a maximum value
 195 if the time delay function $\tau_n^{(i)}$ of each noise source satisfies the
 196 following conditions:

$$197 \quad \tau_n^{(i)} = \frac{|\mathbf{d}_i| \cos \left(\theta_n^{(i)} \right)}{c_0}. \quad (6)$$

198 So, $\theta_n^{(i)}$ will be obtained from $\tau_n^{(i)}$ maximizing the cross-
 199 correlation function. If the noise source's characteristic is white
 200 noise, $R_i(\tau)$ will be the Dirac-delta function. However, the
 201 noise source's characteristic is a broadband signal, and it needs
 a prewhitening method. The radiated noise from the fault state
 insulator contained many spark signals with a 16-ms period, as
 shown in Fig. 1. It can be regarded that the signal is stationary on
 the length over 16 ms. In the present study, the smoothed coher-
 ence transform method [22] was adopted for the prewhitening
 method [23] to minimize the effects of external noise, given by

$$202 \quad R_{x_1 x_2}(\tau) = F^{-1} \left[\frac{X_1 X_2^*}{\sqrt{X_1 X_1^* \bullet X_2 X_2^*}} \right] = F^{-1} [e^{-j\omega \tau_1}]$$

$$203 \quad = \delta(\tau - \tau_1) \quad (7)$$

204 where x_1 and x_2 are the received signals, X_1 and X_2 are their
 respective Fourier transforms, F^{-1} is the inverse Fourier trans-
 form, and $\delta(\bullet)$ is the Dirac-delta function. Cross-correlation

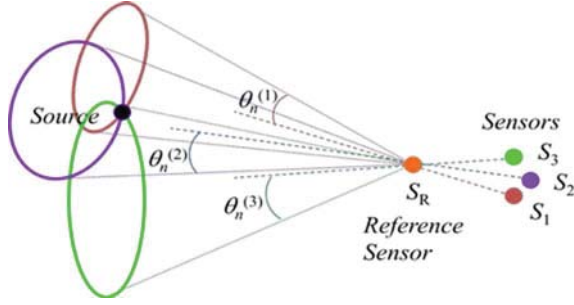


Fig. 3. Intersection of the conical surfaces. n is the angular position forming between a straight line on the sensors and n th noise source and it will be obtained by the cross-correlation function.

205 function analysis of the array sensor's result will be given by a
206 delayed delta signal.

207 B. Noise Source Location Estimation and Arrangement

208 For the noise source location estimation, a 3-D array arrange-
209 ment with four microphones was adopted. By applying (5) to
210 the cross-correlation function between the reference sensor and
211 the arbitrary i th sensor, the time delay index $\tau_n^{(i)}$ from (6) is
212 given by

$$\tau_n^{(i)} = \frac{|\mathbf{d}_i| \cos(\theta_n^{(i)})}{c_0} \quad (8)$$

213 where $\theta_n^{(i)}$ the n th noise source is located in a circular arc, as
214 shown in Fig. 3. It cannot be determined by only one array pair.
215 Thus, at least three pairs of noise sources must be arranged in
216 different planes in the space, so that the source position can be
217 uniquely determined.

218 Let the number of array elements be K ($i = 1, 2, \dots, K$)
219 and the number of the lattice points of the image plane corre-
220 sponding to the noise source azimuth be $M \times N$. Each grid point
221 is given by \mathbf{Z}_{sp} ($s = 1, 2, \dots, M; p = 1, 2, \dots, N$), where
222 the focal length is defined as the distance between the image
223 plane and the reference point, as shown in Fig. 4. Therefore, the
224 time delay index $\tau_{sp}^{(i)}$ between each image point of the image
225 plane \mathbf{Z}_{sp} and the i th sensor pairs is given by

$$\tau_{sp}^{(i)} = \frac{|\mathbf{Z}_{sp} - \mathbf{d}_i| - |\mathbf{Z}_{sp}|}{c_0}. \quad (9)$$

226

227 As the n th sound source is located on the image of the source
228 \mathbf{r}_n , the image of the projected source to the image plane is
229 defined as shown in Fig. 4. Therefore, the image point of the
230 source is given by

$$|\mathbf{z}_{sp} - \mathbf{d}_i| - |\mathbf{z}_{sp}| = |\mathbf{r}_n - \mathbf{d}_i| - |\mathbf{r}_n| = \tau_{sp}^{(i)} c_0. \quad (10)$$

231 When (10) is satisfied, the cross-correlation function $R_i(\tau_{sp}^{(i)})$
232 will have a maximum value. Therefore, the value of $R_i(\tau_{sp}^{(i)})$
233 put on the \mathbf{Z}_{sp} allows an image corresponding to the orientation
234 of the noise source to be obtained.

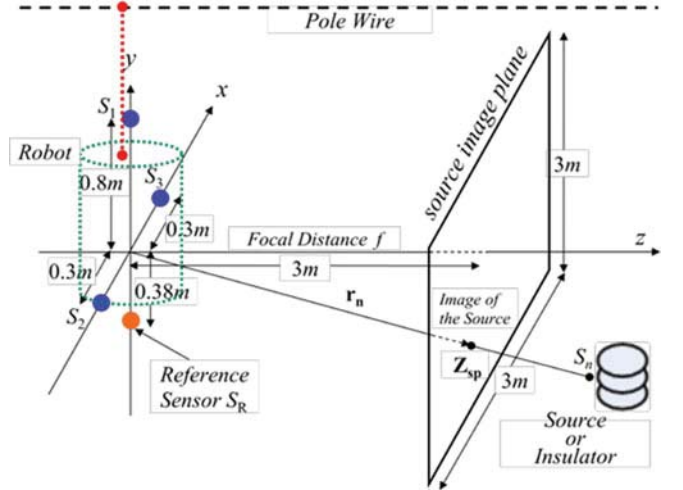


Fig. 4. Array geometry, coordinate, and source image plane. The sound source can be imaged in the source image plane with three sets of time delay, as shown in Fig. 3.

C. Angular Resolution and the Grid Size of the Image Plane

235 In order to separate two adjacent noise sources, the arrange-
236 ment should be designed so that the maximum value of the
237 correlation function can be imaged. It is also necessary for the
238 geometrical interpretation of the geometric distance between
239 the sensors, and the maximum resolution dependent on the band
240 characteristics of the noise source.
241

242 It is assumed that there exist two adjacent noise sources K , L ,
243 and image point positions \mathbf{Z}_k and \mathbf{Z}_l . The time delay index for
244 the i th sensor pair is given by the following equations, respec-
245 tively,
246

$$\tau_k^{(i)} = \frac{|\mathbf{z}_k - \mathbf{d}_i| - |\mathbf{z}_k|}{c_0}, \quad \tau_l^{(i)} = \frac{|\mathbf{z}_l - \mathbf{d}_i| - |\mathbf{z}_l|}{c_0}. \quad (11)$$

247 Using (8) and (11), the difference $\Delta\tau^{(i)}$ in the time delay
248 index for each noise source is given by

$$\Delta\tau^{(i)} = \tau_k^{(i)} - \tau_l^{(i)} = \frac{|\mathbf{d}_i|}{c_0} \left\{ \cos(\theta_k^{(i)}) - \cos(\theta_l^{(i)}) \right\}. \quad (12)$$

249 In addition, let $\theta_k^{(i)} = \theta_l^{(i)} - \Delta\theta$, then (12) is approximated
250 by the following equation:

$$\Delta\tau^{(i)} = \frac{|\mathbf{d}_i|}{c_0} \sin(\theta_l^{(i)}). \quad (13)$$

251 When the bandwidth of the noise source is B , the minimum
252 time difference $\Delta\tau_{\min}^{(i)}$ can be approximated by $1/2B$. It can
253 separate the time delay index corresponding to the maximum
254 value on each noise source on the cross-correlation function.
255 Therefore, $|\Delta\theta|$ is given by

$$|\Delta\theta| > \left| \frac{c_0}{2B |\mathbf{d}_i| \sin(\theta_l^{(i)})} \right|. \quad (14)$$

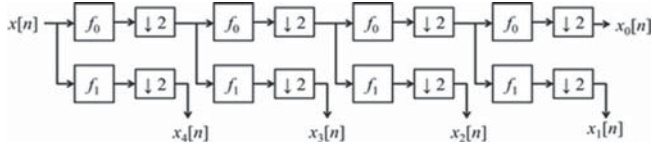


Fig. 5. Multiresolution filter bank. It divides a whole signal into five different width signals in the frequency domains like as 0 kHz ~ 1 kHz, 1 kHz ~ 2 kHz, 2 kHz ~ 4 kHz, 4 kHz ~ 8 kHz, and 8 kHz ~ 16 kHz. $\downarrow 2$ means a factor-of-2 down sampler.

256 In addition, because the lattice point-to-point distance Δz
 257 of the image plane is relatively small compared to the focal
 258 distance f , $\Delta\theta \approx \Delta z/f$. Therefore, Δz in the image plane is
 259 given by

$$|\Delta z| > \left| \frac{f c_0}{2B |d_i| \sin(\theta_l^{(i)})} \right|. \quad (15)$$

260 The resolution and the image plane size of each grid point in
 261 the array is determined by the distance $|d_i|$ between the sensors,
 262 the sound source position $\theta_l^{(i)}$, the bandwidth B , and the focal
 263 distance f of the noise source.

264 D. Feature Extraction Techniques and NN

265 The radiated sound signal from the insulator has a nonuniform
 266 background, and it also contains peak components in a fault state
 267 owing to the microsparks. The amount of background noises
 268 and peak components are important factors to know the signal's
 269 power and peak components' level, respectively. However, the
 270 peak signal can be buried by a nonuniform background signal.
 271 So, both the sector space averaging technique and the filter bank
 272 analysis are applied.

273 In the sector space averaging technique [24], the following
 274 filter is used through the entire frequency spectrum:

$$y[n] = x[n] - \frac{1}{2N} \sum_{k=1}^N \{x[n-k] + x[n+k]\} \quad (16)$$

275 where N is the number for the filter length. The frequency re-
 276 sponse of (16) is the high-pass filter so that the microsparks will
 277 remain. It can also attenuate the slowly varying nonuniform
 278 noise background. $x[n]$ and $y[n]$ are the input and the output
 279 of the filter, respectively. Its frequency characteristic shows an
 280 ideal low-frequency reject filter.

281 The filter bank used to extract the divergence of the entire
 282 frequency spectrum is shown in Fig. 5. The signal is divided
 283 into several separate frequency domains such as 0 kHz ~ 1 kHz
 284 (FB1), 1 kHz ~ 2 kHz(FB2), 2 kHz ~ 4 kHz(FB3), 4 kHz ~
 285 8 kHz(FB4), and 8 kHz ~ 16 kHz(FB5). These five data
 286 domains are used for the input to the curve fitting function.
 287 The algorithm used is the curve fitting library of exponential
 288 models (a single-term exponential) in the MATLAB toolbox.
 289 Among the results, the exponent part will be used for the input
 290 parameters of the NN for the classification.

291 For the classification of the insulators' state, the pattern recog-
 292 nition technique with a NN, as shown in Fig. 6, will be applied.

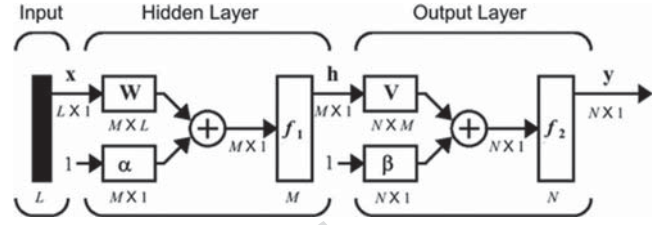


Fig. 6. Block diagram of a NN. It is a multilayer feed-forward networks with one-hidden layer fully connected network. L , M , and N are number of elements in input, hidden, and output layer, respectively [25].

It is a multilayer feed-forward network with one-hidden layer
 fully connected network. L , M , and N are a number of ele-
 ments in the input, hidden, and output layers, respectively. The
 hidden layer has a weight matrix \mathbf{W} , a bias vector α , a de-
 cision function f_1 , and an output vector \mathbf{h} . The output layer
 also has a weight matrix \mathbf{V} , a bias vector β , a decision func-
 tion f_2 , and an output vector \mathbf{y} . The outputs on each layer is
 given by

$$\mathbf{h} = f_1(\mathbf{W}\mathbf{x} + \alpha), \quad \mathbf{y} = f_2(\mathbf{V}\mathbf{h} + \beta). \quad (17)$$

The classification using NN is summarized in the pseudocode
 as follows:

Classification of the insulator using Neural Network

Input: x : input feature data

- 1st data: an exponent part from fitting curve from filter bank results
- 2nd-6th data: amplitudes of harmonic component of 120 Hz
- 7th data: an average from 60 Hz to 660 Hz

Learning/Training: define the weighting on the network
 Repeat following 3 steps to minimize the error

1) output from the hidden layer

for $m = 0$ to $M - 1$ do

$$h_m = f_1\left(\sum^L W_{ml} x_l + \alpha_m\right)$$

end for

2) output from the output layer

for $n = 0$ to $N - 1$ do

$$y_n = f_2\left(\sum^M V_{nm} h_m + \beta_n\right)$$

end for

3) minimize the cost function (sum squared error)

$$C = \sum^l (y_k - y_l)^2$$

Output: y : classification result given by normal or fault

for $p = 0$ to $P - 1$ do

$$[\text{normal or fault}] = \max(\text{logsig}(y_p))$$

end for

P : the number of samples for classification.

The used transfer function of each layer was logsig (logarithmic sigmoid transfer function), the back-propagation network training function was traingd (gradient descent back propagation), and the cost function was sum squared error.

293
294
295
296
297
298
299
300

301
302

303
304
305
306
307

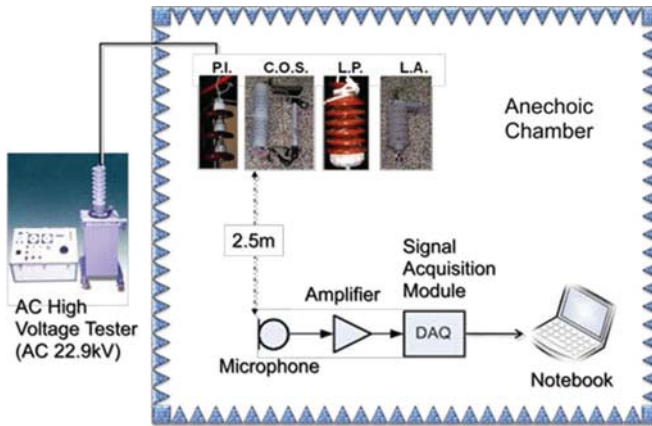


Fig. 7. Block diagram for measurement noises from the insulators. Both the normal state and the fault state of four types of the insulators were measured one by one with sampling frequency 40 kHz in the anechoic chamber. The entire average SPL of ambient noise was 30.51 dB and the average SPL from first to fifth harmonics of 120 Hz was 45.33 dB.

IV. EXPERIMENTAL RESULTS

308

309 The ambient noise in the anechoic chamber was measured
 310 and evaluated for comparison with the insulators' noises in
 311 Section IV-A. The insulators' noises were also measured and
 312 evaluated in Section IV-B, the detection of the fault insulators'
 313 direction with the 3-D array system in Section IV-C, and the NN
 314 for the decision of the fault, or lack thereof, in Section IV-D.

A. Datasets

316 Insulators' noise measurement and analysis methods are de-
 317 veloped. First, the background noise was measured in the an-
 318 echoic chamber with the system, as shown in Fig. 7. As the
 319 acoustic detection system, which is mounted on the robot to
 320 operate at the top of the pole wires, was located less than
 321 3 m from the source to the front end, it was measured with
 322 2.5-m distance in the anechoic chamber. The measurement sys-
 323 tem consisted of four B&K 1/2 in condenser microphones Type
 324 4130, four preamplifiers B&K Type 2642 with the power supply
 325 B&K Type 2810, and a data acquisition device NI USB-9233.
 326 As the received sound's frequency range of the microphone is
 327 5 Hz–12.5 kHz on the response -3 dB, the sampling frequency
 328 was set to be 40 kHz. Both radiation noises of the normal state
 329 and the fault state insulator were measured one by one.

330 Two different analysis methods were attempted by analyzing
 331 the frequency characteristics of the measured time signals using
 332 Fourier transform with a channel 16 384 point data (achieved
 333 from microphone channel 2). The wideband (0–20 kHz) analy-
 334 sis is for looking up the characteristics of the entire frequency
 335 spectrum, evaluating its average level, the harmonics compo-
 336 nents of the 120 Hz, and the peak frequency detection for ex-
 337 tracting the harmonic component in the narrow band (0–1 kHz).

338 Table III shows the dataset to be measured. As the fault state's
 339 standard deviation is larger than the normal state's, the power
 340 of the fault state is also larger than the normal state. In the same
 341 way as ambient noise measurement and analysis, the normal
 342 state and the fault state of the four types of the insulators' noises
 343 were measured and evaluated in Section IV-B.

TABLE III
 TYPES OF INSULATORS FOR MEASUREMENT

Type	Differences	Statistical property: Std (normal/fault)
PI	P.I.1: 2 plates	0.3186/0.6702
	P.I.2: 3 plates	0.2877/0.4351
COS		0.2583/0.3063
LP	L.P.1: company A	0.2565/0.3620
	L.P.2: company B	0.2524/0.3022
LA		0.2679/0.2771

Std: standard deviation.

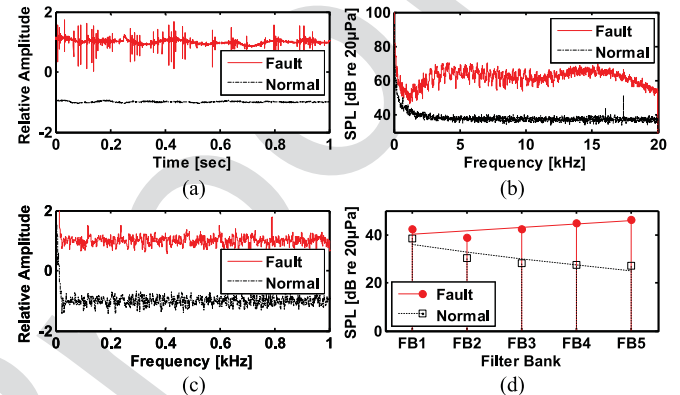


Fig. 8. Comparison between the normal state and the fault state of the PI type 1 (P.I.1): (a) time signal, (b) frequency spectrum, (c) peak detection, and (d) filter bank and its fitting curve. The fault state had values 16.18 and 8.13 dB larger, than those of the normal state in the entire average SPL and the average SPL from first to fifth harmonics of 120 Hz, respectively. The exponent values of normal and fault were -0.09 and 0.03 , respectively.

344 Before the measurement of the insulators' noises, the ambi-
 345 ent noise was measured and evaluated. The results of the ambi-
 346 ent noise's characteristics closely resembled Fig. 8(b)'s normal
 347 state insulator's ambient noise in the wideband analysis and
 348 peak detection. At the frequency spectrum in wideband analy-
 349 sis, it degraded exponentially under 3 kHz and had the flat
 350 characteristics over 3 kHz. There several unexpected peak com-
 351 ponents were found at approximately 800 Hz, 1.6 kHz, 12 kHz,
 352 15 kHz, and 17 kHz. All measured data from insulators also
 353 showed a similar frequency characteristics, so these frequency
 354 components were ignored and not considered in the insulator's
 355 frequency responses. The peak detection result did not have any
 356 considerable characteristics except for the peak at about 800 Hz.
 357 The entire average of the sound pressure level (SPL) on ambi-
 358 ent noise was 30.51 dB and the average SPL from first to fifth
 359 harmonics of 120 Hz was 45.33 dB.

B. Noise Analysis

360

361 The comparison data for both the normal state and the fault
 362 state of the PI type 1 is shown in Fig. 8. Many spike signals
 363 and periodic components were found in the time signal of the
 364 fault state in Fig. 8(a). In the normal state, there are no signifi-
 365 cant components to be considered except some peaks at about
 366 700 Hz, 12 kHz, and 17 kHz like the spectrum of the ambient

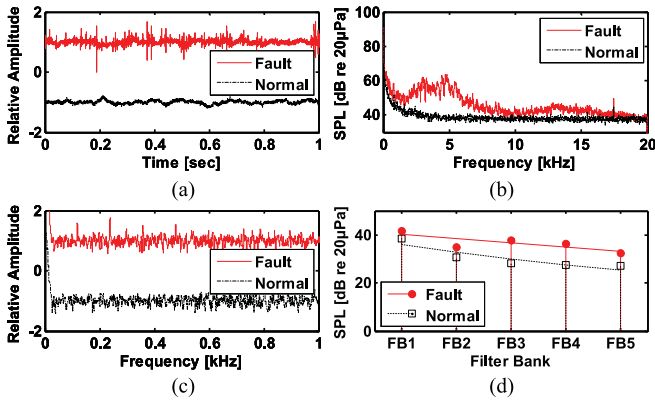


Fig. 9. Comparison between the normal state and the fault state of the COS: (a) time signal, (b) frequency spectrum, (c) peak detection, and (d) filter bank and its fitting curve. The fault state had values 5.33 and 6.52 dB larger than those of the normal state in the entire average SPL and the average SPL from first to fifth harmonics of 120 Hz, respectively. The exponent values of normal and fault were -0.09 and -0.05 , respectively.

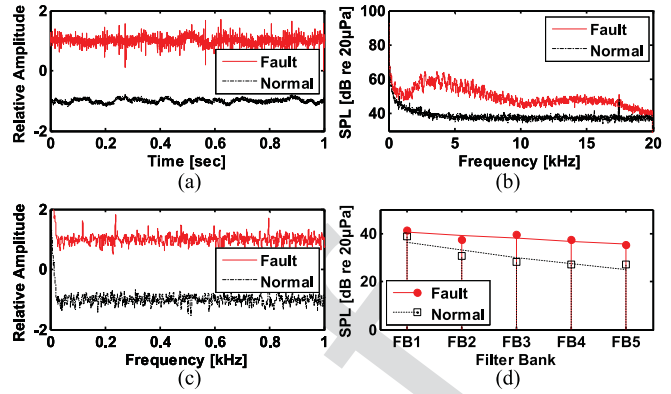


Fig. 10. Comparison between the normal state and the fault state of the LP type 1 (L.P.1): (a) time signal, (b) frequency spectrum, (c) peak detection, and (d) filter bank and its fitting curve. The fault state had values 7.75 and 14.96 dB larger than those of the normal state in the entire average SPL and the average SPL from first to fifth harmonics of 120 Hz, respectively. The exponent values of normal and fault were -0.09 and -0.03 , respectively.

367 noise in the anechoic. The fault state had a larger amplitude than
 368 the normal state through the entire spectrum, especially between
 369 2 and 20 kHz, as shown in Fig. 8(b). There were outstanding
 370 harmonics of 120 Hz by the peak detection in a fault state, as
 371 shown in Fig. 8(c). The entire average SPL in both the normal state
 372 and the fault state were, respectively, 30.38 and 46.56 dB.
 373 The average SPL from first to fifth harmonics of 120 Hz in both
 374 the normal state and the fault state were 47.23 and 59.28 dB, re-
 375 spectively. The normal state had -0.13 and 1.90 dB larger values
 376 than the ambient noise in the entire average SPL and the average
 377 SPL from first to fifth harmonics of 120 Hz, respectively.
 378 The fault state had a value 16.18 dB larger on entire average SPL and
 379 a 8.13 dB larger on average SPL from first to fifth harmonics of
 380 120 Hz than that of the normal state. In the result of the filter
 381 bank and its fitting curve in Fig. 8(d), the exponent part of the
 382 fault state has a larger value than the normal one.

383 Fig. 9 showed the measurement result of the COS. The entire
 384 characteristics of the wideband analysis and the harmonics of
 385 the 120 Hz looked like those of the PI type 1. The entire average
 386 SPL in the normal state was 30.52 dB and 35.86 dB in the
 387 fault state. The average SPL from first to fifth harmonics of
 388 120 Hz in both the normal state and the fault state were 40.10 and
 389 46.62 dB, respectively. The normal state had 0.02 and 0.19 dB
 390 larger values than the ambient noise in the entire average SPL
 391 and the average SPL from first to fifth harmonics of 120 Hz.
 392 The fault state had values 5.33 and 6.52 dB larger than that
 393 of the normal state in average of the entire spectrum and the
 394 harmonics, respectively.

395 Fig. 10 showed the measurement result of the LP type 1.
 396 The entire average SPL in both the normal state and the fault
 397 state were 30.31 and 38.06 dB, respectively. The average SPL
 398 from the first to fifth harmonics of 120 Hz in both the normal
 399 state and the fault state were 45.44 and 62.11 dB, respectively.
 400 The normal state had -0.19 and 0.12 dB larger values than the
 401 ambient noise in the entire average SPL and the average SPL
 402 from first to fifth harmonics of 120 Hz, respectively. The fault
 403 state had values 7.75 and 14.96 dB larger than that of the normal

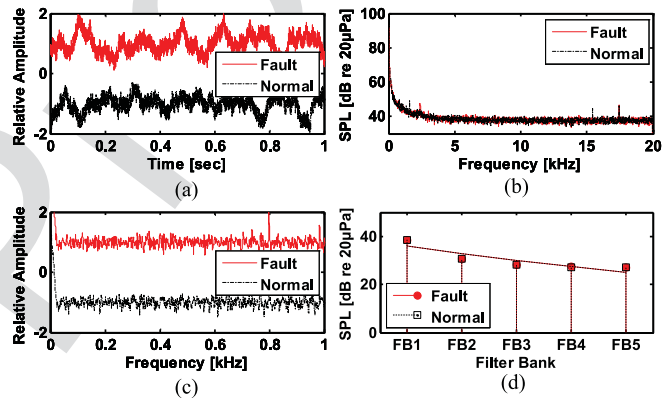


Fig. 11. Comparison between the normal state and the fault state of the LA: (a) time signal, (b) frequency spectrum, (c) peak detection, and (d) filter bank and its fitting curve. The fault state had values 0.05 and -0.28 dB larger than those of the normal state in the entire average SPL and the average SPL from first to fifth harmonics of 120 Hz, respectively. Both exponent values of fault and normal were -0.09 .

state in the entire average SPL and the average SPL from first
 404 to fifth harmonics of 120 Hz, respectively. 405

406 Fig. 11 showed the measurement result of the lightning ar-
 407 rester. The characteristics were entirely different from the former
 408 three insulators. In the time signal, the difference between the
 409 fault state and the normal state was not found. In the wide-
 410 band analysis and the harmonics of the 120 Hz, the insulator's
 411 spark also could not be determined. In addition, the frequency
 412 spectrums did not show any difference between each other, so it
 413 could not be detected by the difference in results of detection of
 414 a peak in a narrow band. The entire average SPL in the normal
 415 state was 30.55 dB, and 30.60 dB in the fault state. The average
 416 SPL from first to fifth harmonics of 120 Hz in both the normal
 417 state and the fault state were 45.37 and 45.31 dB, respectively.
 418 The normal state had 0.05 and 0.05 dB larger values than the
 419 ambient noise in the entire average SPL and the average SPL
 420 from first to fifth harmonics of 120 Hz. The fault state had val-
 421 ues 0.05 and -0.28 dB larger than that of the normal state in

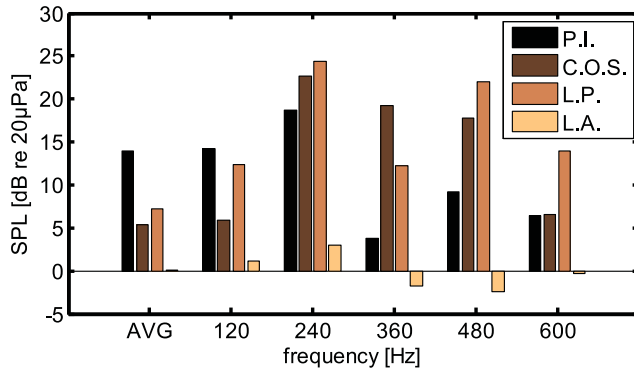


Fig. 12. Differences between the normal state and the fault state of the insulators. AVG means the mean total power in entire frequency response. Except LA, the SPL of the fault states are larger than those of the normal states.

TABLE IV
COMPARISON OF ALL RESULTS

Noise source (normal/fault)	Entire average SPL	Average SPL of harmonics of 120 Hz	Exponent value of fitting curve
Ambient noise	30.51	45.33	-0.09
PI	30.38	47.23	-0.09
46.56	59.28	-0.03	
COS	30.52	40.10	-0.09
35.86	46.62	-0.05	
LP	30.31	45.44	-0.09
38.06	62.11	-0.03	
LA	30.55	45.37	-0.09
30.60	45.31	-0.09	

All SPL's units are in dB.

the entire average SPL and the average SPL from first to fifth harmonics of 120 Hz, respectively. This meant that to figure out the fault state of the lightning arrester would be more difficult than other insulators. A possible way to determine the fault state of the lightning arrester would be diagnosis by thermal infrared camera, as shown in [2].

The difference between the normal state and the fault state of the insulators was shown in Fig. 12. AVG meant the entire average SPL of wideband analysis, and the other was the SPL of the harmonics of the 120 Hz in horizontal axis. In AVG, except for the lightning arrester, the fault state's values were larger than those of the normal state. The harmonics of the 120 Hz were also larger, except for the lightning arrester. From these two apparent results—the wideband analysis and the harmonics of the 120 Hz, the possibility of detecting the fault state of the insulators can be found, except for the lightning arrester. It can be concluded that the fault state's values are larger than the normal state's in both total average and 120 Hz harmonic components, as shown in Fig. 12. In the exponent value of curve fitting from result of filter bank, it was found that values of fault states were larger than normal state. For ease of comparison, results were summarized and shown in Table IV.

C. Noise Source Location

Per the previous section's result, the radiated noise had two significant features in the total average and 120 Hz harmonics

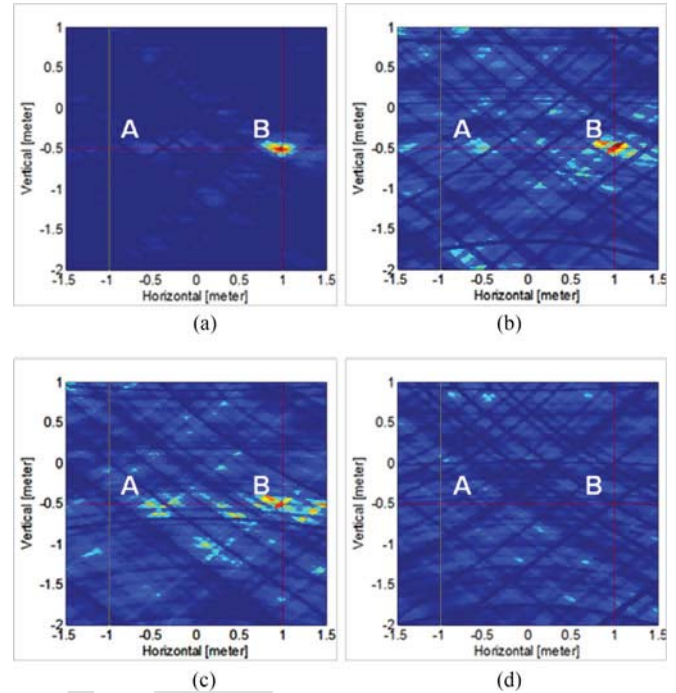


Fig. 13. Source localization results: (a) PI, (b) COS, (c) LP, and (d) LA. The normal and fault state insulator are located in A and B, respectively. Three different type fault insulators were detected, except LA. The rectangular coordinates (x, y, z) m of A and B are $(-1.0, -0.5, 3.0)$ m and $(1.0, -0.5, 3.0)$ m, respectively.

components that could be detected by the microphone. The noise source location was evaluated by 3-D microphone array, as shown in Fig. 4. The source image plane's size is 3 m width and 3 m height. The number of the lattice points $M \times N$ were chosen as 200. So the size of image on source image plane has 15-mm ($= 3 \text{ m}/200$ points) resolutions.

The insulator would be in a slightly lower position below the robot, so the reference sensor was chosen to be the nearest to it, as shown in Fig. 4. For the noise source location estimation with the 3-D microphone system, two insulators' locations were estimated at the same time. The normal and fault state insulators were located in A and B, respectively. The rectangular coordinates (x, y, z) m of A and B are $(-1.0, -0.5, 3.0)$ m and $(1.0, -0.5, 3.0)$ m, respectively. The results are shown in Fig. 13. The left cross line represents the position of a normal state insulator and the right cross line represents the position of a fault state insulator.

The entirety of the normal insulators was not detected. Meanwhile, the first three fault insulators were detected except for (d) lightning arrester (LA). Distance error is evaluated as the Euclidean norm between a source's coordinate B and the estimated coordinate, as shown in Table V. The first three insulators were very close to source B and the differences came from the value of the spectrum's average.

D. Fault Detection

The fault detection was evaluated using a NN. Per the results in Section IV-B, the combinations of total average and 120 Hz

TABLE V
FAULT LOCATION SOURCES ESTIMATION

Type	Auctual coordinate	Estimated coordinate	Distance error (m)
PI	(1.0, 0.5)	(0.975, 0.515)	0.03
COS	(1.0, 0.5)	(1.110, 0.530)	0.11
LP	(1.0, 0.5)	(1.125, 0.530)	0.12
LA	(1.0, 0.5)	NON	N/A

474 harmonic components were used for the input data. The datasets
475 for the input layer were figured out and chosen by the following:

- 476 1) first data: the exponent part of the exponential curve fit-
477 ting from the filter bank results;
- 478 2) second to sixth data: amplitudes of the harmonic compo-
479 nent of 120 Hz;
- 480 3) seventh data: an average from 60 to 660 Hz.

481 For the NN, the numbers of layers were chosen as 7, 30, and
482 2 for the input, the hidden, and the output layer, respectively.
483 These numbers were empirically chosen and then validated after
484 variable numerical setting. The number of input layers depends
485 on the frequency characteristics as given by the output of filter
486 bank, peak signals, and average level. The number of output
487 layers depends on the results from classification as given by
488 normal or fault states.

489 The training data was the average of each insulator’s one
490 second length signal achieved from microphone channel 2. The
491 data length was about 4 s in length, so that each average was
492 obtained from four datasets. For the tolerance of the reference
493 signal, the data was multiplied by 1.1 and divided by 1.1. Total
494 training dataset resulted in six datasets from each insulator.
495 The input data for the classification were 20 datasets, which
496 consisted of four 1-s-length signals and a 4-s-length signal from
497 two different microphone channels (achieved from channel 1
498 and channel 4).

499 The fault detection was evaluated from the four datasets using
500 the confusion matrix in Fig. 14. It shows the performance of
501 the classification algorithm with a table layout. It contains true
502 positives (actually fault and classification output is also fault
503 on first row/first column), false negatives (actually normal but
504 classification output is fault on first row/second column), false
505 positives (actually fault but classification output is normal on
506 second row/first column), and true negatives (actually normal
507 and classification output is also normal on second row/second
508 column). There is one failure case regarding normal state as
509 fault state on second row/first column in (a) PI and (b) COS So
510 the total accuracy would be 95% (adding 10/10 in true positives
511 and 9/10 in true negatives). The ratio 100% illustrates no error in
512 classification. The highest detection ratio was 100% for (c) LP
513 and others were relatively more than 95%, except (d) LA. The
514 spectrum in LA was hard to distinguish between normal and
515 fault state, thus, it reached 75% (adding 8/10 in true positives
516 and 7/10 in true negatives).

517 The fault detection was also evaluated using other criteria cal-
518 culated in Table V. The F₁ score, accuracy, and Matthews cor-
519 relation coefficient (MCC) [26] were used for the four datasets.
520 Table VI shows that these statistical values are consistently high
521 among three metrics, especially the first three datasets. These

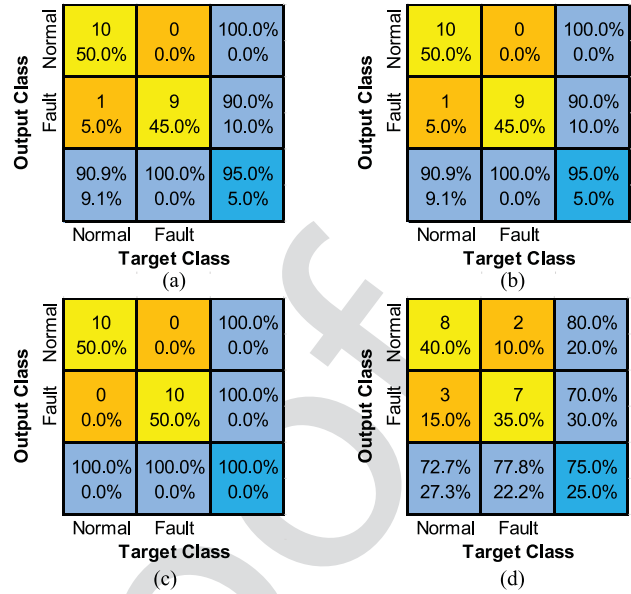


Fig. 14. The confusion matrix corresponding to Table II. (a) PI (b) COS (c) LP (d) LA.

TABLE VI
STATISTICAL EVALUATION

Type	F ₁ score	Accuracy	MCC
PI	95.24	95.00	0.90
COS	95.24	95.00	0.90
LP	100.00	100.00	1.00
LA	76.19	75.00	0.50

The ratio 100% or 1.0 illustrate no error in classification.

522 statistical evaluations validated that the proposed acoustic fault
523 detection system from insulators’ radiation noises was feasible.

524 To represent the effectiveness on our system with comparison
525 with [2], there are differences in the following three areas. First,
526 there were represented analysis results with wideband analy-
527 sis, peak detection using sector space averaging technique, and
528 exponent value from the curve fitting. Second, in source local-
529 ization, comparing the results of [2] shown in Table V, it can be
530 seen that there is almost no distance error. Also, the visual effect
531 can be obtained by indicating on the source image plane where
532 the noise is generated, as shown in Fig. 13. The noise source
533 was detected with 100.0% accuracy for three typical conditions.
534 Finally, from the analysis results, the fault detection was deter-
535 mined by NN to diagnose the state automatically. The highest
536 detection ratio was 100% and others were relatively more than
537 95%, except LA.

V. CONCLUSION

538
539 In this paper, radiation noises were measured and analyzed
540 from both the normal state insulators and the fault state insula-
541 tors in the anechoic chamber. Two apparent results were found
542 from their frequency spectrums—120 Hz harmonic components
543 and higher average noise levels than normal state ones. The
544

544 technique for the direction estimation of the fault state insulator
 545 using the cross correlation from the 3-D array microphones was
 546 also introduced. Finally, the classification technique using a NN
 547 was shown. It was also concluded that acoustic fault detection
 548 techniques are useful in the detection of insulator faults and the
 549 estimation of the direction of the fault state insulators. In addition,
 550 it was also demonstrated that the fault state of the lightning
 551 arrester is not distinguished from the normal state of that.

552 Future work includes larger scale datasets under the real out-
 553 door environment with more radiation noise data and a high
 554 accuracy NN.

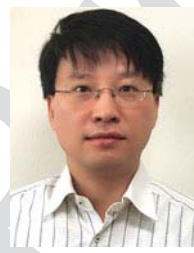
555 ACKNOWLEDGMENT

556 The authors would like to thank L. Linkous and A. Huynh for
 557 proofreading and helping to improve the paper.

558 REFERENCES

- 559 [1] W. R. Vincent, G. F. Munsch, R. W. Adler, and A. A. Parker, "The Mitiga-
 560 tion of Radio Noise from External Sources at Radio Receiving Sites, 6th
 561 ed. Monterey, CA, USA: Naval Postgraduate School, 2007.
- 562 [2] H. Ha, S. Han, and J. Lee, "Fault detection on transmission lines using a
 563 microphone array and an infrared thermal imaging camera," *IEEE Trans.*
 564 *Instrum. Meas.*, vol. 61, no. 1, pp. 267–275, Jan. 2012.
- 565 [3] K.-C. Park and J. R. Yoon, "Analysis of the insulators' radiation noises
 566 for error detections," in *Proc. Symp. Ultrason. Electron.*, 2009, vol. 30,
 567 pp. 249–250.
- 568 [4] J. B. Dixit and A. Yadav, *Electric Power Quality*. New Delhi, India: Univ.
 569 Sci. Press, 2010, p. 2.
- 570 [5] *IEEE Recommended Practice for Monitoring Electric Power Quality*,
 571 IEEE Standard 1159-2009, 2009.
- 572 [6] A. Vidal *et al.*, "Assessment and optimization of the transient response of
 573 proportional-resonant current controllers for distributed power generation
 574 systems," *IEEE Trans. Ind. Electron.*, vol. 60, no. 4, pp. 1367–1383,
 575 Apr. 2013.
- 576 [7] M. Savaghebi, A. Jalilian, J. C. Vasquez, and J. M. Guerrero, "Autonomous
 577 voltage unbalance compensation in an islanded droop-controlled micro-
 578 grid," *IEEE Trans. Ind. Electron.*, vol. 60, no. 4, pp. 1390–1402, Apr. 2013.
- 579 [8] M. Valtierra-Rodríguez, R. De Jesus Romero-Troncoso, R. A. Osornio-
 580 Rios, and A. Garcia-Perez, "Detection and classification of single and
 581 combined power quality disturbances using neural networks," *IEEE Trans.*
 582 *Ind. Electron.*, vol. 60, no. 5, pp. 2473–2482, May 2014.
- 583 [9] D. Chen, J. Zhang, and Z. Qian, "An improved repetitive control scheme
 584 for grid-connected inverter with frequency-adaptive capability," *IEEE*
 585 *Trans. Ind. Electron.*, vol. 60, no. 2, pp. 814–823, Feb. 2013.
- 586 [10] Y. F. Wang and Y. W. Li, "Three-phase cascaded delayed signal cancella-
 587 tion PLL for fast selective harmonic detection," *IEEE Trans. Ind.*
 588 *Electron.*, vol. 60, no. 4, pp. 1452–1463, Apr. 2013.
- 589 [11] J. Wang, Q. He, and F. Kong, "Adaptive multiscale noise tuning stochastic
 590 resonance for health diagnosis of rolling element bearings," *IEEE Trans.*
 591 *Instrum. Meas.*, vol. 64, no. 2, pp. 564–577, Feb. 2015.
- 592 [12] S. Choi, B. Akin, M. M. Rahimian, and H. A. Toliyat, "Performance-
 593 oriented electric motors diagnostics in modern energy conversion sys-
 594 tems," *IEEE Trans. Ind. Electron.*, vol. 59, no. 2, pp. 1266–1277, Feb. 2012.
- 595 [13] B. Akin, S. Choi, U. Orguner, and H. A. Toliyat, "A simple real-time
 596 fault signature monitoring tool for motor-drive-embedded fault diagnosis
 597 systems," *IEEE Trans. Ind. Electron.*, vol. 58, no. 5, pp. 1990–2001,
 598 Jun. 2011.
- 599 [14] J. Kim and B. You, "Fault detection in a microphone array by intercorre-
 600 lation of features in voice activity detection," *IEEE Trans. Ind. Electron.*,
 601 vol. 58, no. 6, pp. 2568–2571, Jun. 2011.
- 602 [15] S. A. Zekavat and R. M. Buehrer, *Handbook of Position Location: Theory,*
 603 *Practice and Advances*, 1st ed. Hoboken, NJ, USA: Wiley, 2011.
- 604 [16] R. A. Mucci, "A comparison of efficient beamforming algorithms," *IEEE*
 605 *Trans. Acoust., Speech, Signal Process.*, vol. ASSP-32, no. 3, pp. 548–558,
 606 Jun. 1984.
- 607 [17] B. Friedlander, "A sensitivity analysis of the MUSIC algorithm," *IEEE*
 608 *Trans. Acoust., Speech, Signal Process.*, vol. 38, no. 10, pp. 1740–1751,
 609 Oct. 1990.

- [18] C. H. Knapp and G. C. Carter, "The generalized correlation method for
 estimation of time delay," *IEEE Trans. Acoust., Speech, Signal Process.*,
 vol. ASSP-24, no. 4, pp. 320–327, Aug. 1976.
- [19] I. Jouny, F. D. Garber, and R. L. Moses, "Radar target identification using
 the bispectrum: A comparative study," *IEEE Trans. Aerosp. Electron.*
Syst., vol. 31, no. 1, pp. 69–77, Jan. 1995.
- [20] G. Moschioni, B. Saggin, and M. Tarabini, "3-D sound intensity mea-
 surements: Accuracy enhancements with virtual-instrument-based tech-
 nology," *IEEE Trans. Instrum. Meas.*, vol. 57, no. 9, pp. 1820–1829,
 Sep. 2008.
- [21] J. D. Maynard, E. G. Williams, and Y. Lee, "Nearfield acoustic holo-
 graphy: I. Theory of generalized holography and the development of
 NAH," *J. Acoust. Soc. Amer.*, vol. 78, pp. 1395–1413, 1985.
- [22] G. C. Carter, A. H. Nuttall, and P. Cable, "The smoothed coherence
 transform," *Proc. IEEE*, vol. 61, no. 10, pp. 1497–1498, Oct. 1973.
- [23] M. P. Oliveri, "A broadband signal processor for acoustic imaging using
 ambient noise," M.S. thesis, Dept. Ocean Eng., Florida Atlantic Univ.,
 Boca Raton, FL, USA, 1994.
- [24] R. O. Nielsen, *Sonar Signal Processing*. Norwood, MA, USA: Artech
 House, 1991.
- [25] Neural Network Toolbox. [Online]. Available: <https://www.mathworks.com/help/nnet/index.html>
- [26] D. M. W. Powers, "Evaluation: From precision, recall and F-measure to
 ROC, informedness, markedness & correlation," *J. Mach. Learn. Technol.*,
 vol. 2, pp. 37–63, 2011.



Kyu-Chil Park received the B.S. and M.S. de-
 grees from the Department of Electronic En-
 gineering, Pukyong National University, Busan,
 South Korea, in 1993 and 1995, respectively,
 and the Ph.D. degree from the Graduate School
 of Natural Science and Technology, Okayama
 University, Okayama, Japan, in 2000.

Since 2002, he has been a Professor in the
 Department of Information and Communications
 Engineering, Pukyong National University. His
 research interests include underwater acoustic
 signal processing, adaptive signal processing, numerical analysis, opti-
 mization, and inverse problems in engineering.



Yuichi Motai (S'00–M'03–SM'12) received the
 B.Eng. degree in instrumentation engineering
 from Keio University, Tokyo, Japan, in 1991, the
 M.Eng. degree in applied systems science from
 Kyoto University, Kyoto, Japan, in 1993, and the
 Ph.D. degree in electrical and computer engi-
 neering from Purdue University, West Lafayette,
 IN, USA, in 2002.

He is currently an Associate Professor of elec-
 trical and computer engineering at Virginia Com-
 monwealth University, Richmond, VA, USA. His
 research interests include the broad area of sensory intelligence, par-
 ticularly in medical imaging, pattern recognition, computer vision, and
 sensory-based robotics.



Jong Rak Yoon received the M.S. and Ph.D. de-
 grees in ocean engineering from Florida Atlantic
 University, Boca Raton, FL, USA, in 1990.

From 1979 to 1985, he was a Research Sci-
 entist with the Agency for Defense Development.
 Since 1990, he has been a Faculty Member in
 the Department of Information and Communi-
 cations Engineering, Pukyong National Univer-
 sity, Busan, South Korea. His research interests
 include underwater acoustics and underwater
 acoustic signal processing with an emphasis on
 underwater acoustic signal measurement/analysis, classification, and
 underwater acoustic communication.

Dr. Yoon is a member of the Acoustical Society of America.

Q1

Q2

Q3

678